micromachines

https://www.mdpi.com/journal/micromachines

Impact factor = 3.523

Accepted December 8th 2022

Analysis of nonlinear convection-radiation in chemically reactive Oldroyd-B nanoliquid configured by a stretching surface with Robin conditions: applications in nano-coating manufacturing

Muhammad Nasir[1], Muhammad Waqas[2,*], O. Anwar Bég[3] and Nurnadiah Zamri[1]

[1]Faculty of Informatics and Computing, University Sultan Zainal Abidin, Besut Campus, 22200 Besut, Terengganu, Malaysia.

[2]NUTECH School of Applied Science and Humanities, National University of Technology, Islamabad 44000, Pakistan.

[3]Professor and Director-Multi-Physical Engineering Sciences Group (MPESG), Corrosion/Coatings Lab, Room 3-08, SEE Bldg, Mechanical Engineering, Salford University, Manchester, M54WT, UK.

**Correspondence: muhammadwaqas@nutech.edu.pk (M. Waqas).*

Abstract: Motivated by emerging high-temperature manufacturing processes deploying nano-polymeric coatings, the present communication studies nonlinear thermally radiative Oldroyd-B viscoelastic nanoliquid stagnant-point flow from a heated vertical stretching permeable surface. Robin (mixed derivative) conditions are utilized to better represent coating fabrication conditions. The nanoliquid analysis is based on Buongiorno's two-component model which elaborates Brownian movement and thermophoretic attributes. Nonlinear buoyancy force and thermal radiation formulations are included. Chemical reaction (constructive and destructive) is also considered since coating synthesis often features reactive transport phenomena. Via a similarity approach, an ordinary differential equation model is derived from the primitive partial differential boundary value problem. Analytical solutions are achieved employing homotopy analysis scheme. The influence of emerging dimensionless quantities on transport characteristics is comprehensively elaborated with appropriate data. The obtained analytical outcomes are compared with available limiting studies and good correlation is achieved. The computations show that the velocity profile is diminished with increasing relaxation parameter whereas it is enhanced when retardation parameter is increased. Larger thermophoresis parameter induces temperature and concentration enhancement. The heat and mass transfer rates at the wall are increased with an increment in temperature ratio and first order chemical reaction parameters while contrary effects are observed for larger thermophoresis, fluid relaxation and Brownian motion parameters. The simulations find applications in stagnation nano-polymeric coating of micromachines, robotic components and sensors.

Keywords: *Nonlinear mixed convection; Stagnant-point flow; Stretching permeable surface; Oldroyd-B nanoliquid; Chemical reaction; Nonlinear thermal radiation; Homotopy analysis scheme; nano-coating fabrication.*

Nomenclature

β_t	Nonlinear thermal convection parameter;	D_B	Brownian diffusion coefficient ($\mathrm{m}^2.\mathrm{s}^{-1}$);
D_t	Thermophoretic diffusion coefficient ($\mathrm{m}^2.\mathrm{s}^{-1}$);	u, v	velocity components (ms^{-1});
θ_R	temperature ratio parameter;	C_f	Skin friction coefficient;
β_c	Nonlinear concentration convection parameter;	γ_1	Thermal Biot number;
T	Fluid temperature (K);	Re_x	Local Reynolds number;
Pr	Prandtl number;	θ	Dimensionless temperature;
R	radiation parameter;	ϕ	Volume fraction of nanoparticles;
A	ratio of rates;	ρ_f	Density of base-fluid (kgm^{-3});
C_∞	Ambient fluid concentration;	N	buoyancy ratio parameter;
T_∞	Ambient fluid temperature (K);	f	Dimensionless velocity;
Nu_x	Local Nusselt number;	N_t	Thermophoresis parameter;
N_b	Brownian motion parameter;	γ_2	Solutal Biot number;
η	Similarity variable;	x, y	coordinate axes (m)

1 Introduction

Boundary-layer flows configured by moving surfaces have remarkable industrial applications, including fiber technology, aerodynamic extrusion of plastic sheets, melting spinning, enhanced recovery of petroleum resources, artificial fibers, the hot rolling, glass-fiber, paper manufacturing, and polythene items production. The theory of boundary layer flow caused by a continuously flat surface moving with constant velocity was first described by Sakiadis [1]. Crane [2] modeled boundary-layer stretching flow and computed closed-form solutions. Various researchers extended the analyses of Sakiadis [1] and Crane [2] under diverse physical aspects. For instance, Govindaraj et al. [3] presented the 2D water type boundary-layer flow confined by moving exponential vertical surface and analyzed the impact of Prandtl number and variable viscosity. Ibrahim and Gadisa [4] explored the aspects of suction/injection in micropolar nanoliquid boundary-layer flow based on improved theories of heat-mass transfer. Rajput et al. [5] inspected the effectiveness of porous medium on magnetohydrodynamics boundary-layer flow across an exponentially stretched surface and solved it numerically by applying the shooting technique. The phenomenon of boundary-layer flow over a vertical Riga plate with magnetohydrodynamics (MHD) and viscous dissipation has been carried out by Eldabe et al. [6]. Dawar et al. [7] explored the mixed convective boundary-layer flow featuring chemically reactive micropolar liquid over a stretchable surface with Joule heating. Nadeem et al. [8] numerically described the 2-D boundary-layer flow considering Buongiorno nanoscale model past a nonlinear extending surface capturing porous medium impact. Further analyses in this direction are mentioned in Refs. [9-20].

Researchers at present are enthusiastic to scrutinize viscoelastic liquids due to their broad engineering and industrial applications. These liquids are used in prescribed medications [21], colloidal matter, physiological, volatiles, food manufacturing [22, 23], oil reservoir engineering, fabric technologies, melts of polymeric, thermal circuit processing [24, 25] and chemical/nuclear industries [26]. Stress and strain are not enough to distinguish between the different characteristics of these liquids. For diverse rheological characteristics, numerous constitutive relationships have been developed. In current study, the Oldroyd-B liquid model has been considered which elaborates the effects of memory and elasticity which are common features in many biological and polymeric liquids deployed in modern coating systems. In addition, this model also captures relaxation and retardation time effects. This model reduces to the Maxwell fluid in the absence of retardation time. Furthermore, when both relaxation and retardation times fluid are omitted, the Oldroyd-B model retracts to the classical (viscous fluid) Newtonian model. This model has been implemented by various researchers under diverse flows assumptions. For illustration, Hafeez et al. [27] employed the bvp4c scheme design in MATLAB software to compute numerical solutions for Cattaneo-Christov based Oldroyd-B nanoliquid towards a spinning disc. Rana et al. [28] presented mathematical analysis of

Oldroyd-B nanofluid configured by permeable surface considering gyrotactic microorganisms. Bioconvection impact in Oldroyd-B liquid slip flow persuaded by heated surface is evaluated by Khan et al. [29]. They concluded that solutal profile decreases with increasing Schmidt number and retardation time constant. Ali et al. [30] considered Soret-Dufour and MHD effects in Cattaneo-Christov heat-mass flux models based Oldroyd-B nanoliquid rotating flow employing finite element scheme. Significance of Robin conditions in chemically reactive radiated Oldroyd-B nanoliquid considering thermophoretic and Brownian diffusion effects is elaborated by Irfan et al. [31]. They noted that solutal and thermal Biot numbers have the same influence on concentration and temperature field respectively. Yasir et al. [32] computed homotopic convergent solutions for Oldroyd-B liquid stretched flow subjected to energy transport Recent studies related to Oldroyd-B fluid have been reported in Refs. [33-37].

This analysis aims to extend the research presented by Nasir et al. [38] for nonlinear radiative Robin conditions based Oldroyd-B nanoliquid confined by stretchable porous vertical surface. Nonlinear mixed convective flow in the stagnation region is formulated. Mass transfer effects are explored considering chemical reaction. Undoubtedly, various computational (analytical, numerical) schemes [39-47] are available in existing literature. Here, the nonlinear problems are computed via homotopic approach [48-50] for convergent series solutions. Moreover, graphical depictions of some key findings with a detailed discussion have also been incorporated. The applications of the present non-Newtonian nanofluid stagnation model includes coating manufacturing processes for biomimetic sensors [51], optical fiber nanocoatings [52,53] and micro-robot surface protection [54, 55]. The *key objective* of the present study is to simultaneously consider multiple effects which feature in real manufacturing stagnation flows for nanopolymer coatings including complex thermal convective wall boundary conditions, rheology, high temperature (radiative flux), Brownian motion and thermophoresis. These have not been addressed previously with the Oldroyd-B viscoelastic model.

2. Mathematical model

Consider the nonlinear mixed convective flow in the stagnation region of Oldroyd-B nanoliquid confined by a heated permeable vertical surface, as a model of manufacturing coating deposition of a nanopolymer. The rheological nature of many polymeric nanocoatings requires a robist non-Newtonian model which can simulate real effects including relaxation and retardation, for which the Oldroyd-B model is an excellent candidate. The nanoliquid model presented by Buongiorno [8] featuring Brownian diffusion and thermophoresis effects is utilized since it provides two-component (thermosolutal) framework for analysis. Nonlinear radiative aspect along with Robin conditions is considered to represent high temperature manufacturing conditions and complex wall conditions in coating deposition processes. Mass transfer effects are explored considering chemical reaction which is also common in nanomaterial polymeric coating synthesis. The physical model is visualized in **Fig. 1** with robotic sensor surface deposition applications on the left and the stagnation flow regime simulated on the right. The governing conservation equations under the considered effects are [34]:

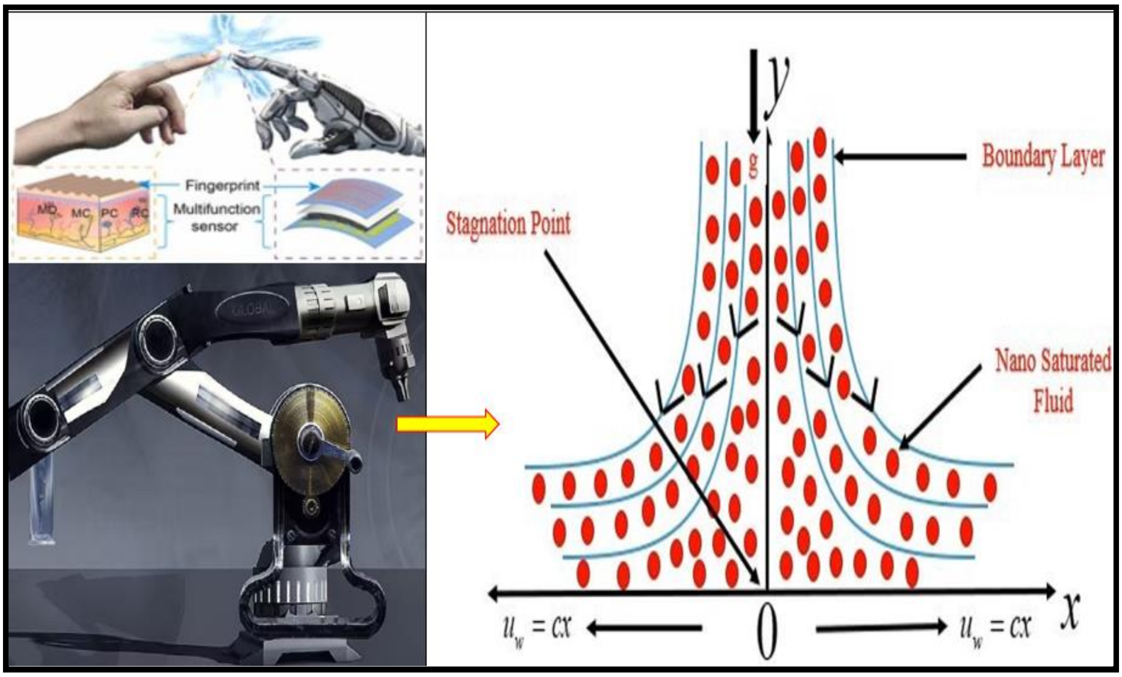

Figure 1. Left robot-controlled micromachine stagnation coating of functional nanopolymers, right – 2-D stagnation flow model for Oldroyd-B nanopolymer deposition on robotic sensor.

$$\frac{\partial u}{\partial x} + \frac{\partial v}{\partial y} = 0, \tag{1}$$

$$\begin{cases} u\dfrac{\partial u}{\partial x} + v\dfrac{\partial u}{\partial y} + \lambda_1\left(u^2\dfrac{\partial^2 u}{\partial x^2} + v^2\dfrac{\partial^2 v}{\partial y^2} + 2uv\dfrac{\partial^2 u}{\partial x \partial y}\right) = \nu\left(\dfrac{\partial^2 u}{\partial y^2} + \lambda_2\left(\dfrac{\partial^3 u}{\partial x \partial y^2}u - \dfrac{\partial u}{\partial x}\dfrac{\partial^2 u}{\partial y^2} - \dfrac{\partial u}{\partial y}\dfrac{\partial^2 v}{\partial y^2} + v\dfrac{\partial^3 u}{\partial y^3}\right)\right) \\ +u_e\dfrac{du_e}{dx} + g\left\{\Lambda_1\left(T-T_\infty\right) + \Lambda_2\left(T-T_\infty\right)^2\right\} + g\left\{\Lambda_3\left(C-C_\infty\right) + \Lambda_4\left(C-C_\infty\right)^2\right\}, \end{cases} \tag{2}$$

$$u\frac{\partial T}{\partial x}+v\frac{\partial T}{\partial y}=\alpha\frac{\partial^2 T}{\partial y^2}+\tau\left[D_B\frac{\partial C}{\partial y}\frac{\partial T}{\partial y}+\frac{D_T}{T_\infty}\left(\frac{\partial T}{\partial y}\right)^2\right]+\frac{16\sigma^*}{3k^*\left(\rho c\right)_f}\frac{\partial}{\partial y}\left(T^3\frac{\partial T}{\partial y}\right), \quad \textbf{(3)}$$

$$u\frac{\partial C}{\partial x}+v\frac{\partial C}{\partial y}=D_B\frac{\partial^2 C}{\partial y^2}+\frac{D_T}{T_\infty}\frac{\partial^2 T}{\partial y^2}-K_1\left(C-C_\infty\right) \quad \textbf{(4)}$$

$$u=u_w(x)=cx, v=v_w, -k\frac{\partial T}{\partial y}=-h_s\left(T_f-T\right), -D_B\frac{\partial C}{\partial y}=-h_c\left(C_f-C\right). \textbf{ at } y=0, \quad \textbf{(5)}$$

$$u\to u_e(x)=ex, T\to T_\infty, C\to C_\infty \textbf{ when } y\to\infty. \quad \textbf{(6)}$$

Here $\nu\left(=\frac{\mu}{\rho_f}\right)$ denotes the kinematic viscosity of sheet, ρ_f liquid density, μ dynamic viscosity , λ_1 relaxation time, k thermal conductivity, $u_e\left(x\right)$ free stream velocity, g gravitational acceleration, T_∞ ambient temperature liquid, D_T thermophoresis diffusion coefficient, Λ_1 thermal expansion coefficient, heat capacity ratio $\tau=\frac{(\rho c)_P}{(\rho c)_f}$ with liquid heat $(\rho c)_f$, nanoparticles effective heat capacity $(\rho c)_p$, σ^* Stefan-Boltzmann constant, D_B Brownian diffusion coefficient , λ_2 retardation time, K_1 reaction rate, k^* mean absorption coefficient, $\alpha=\frac{k}{(\rho c)_f}$ thermal diffusivity, T liquid temperature, $\left(u_w(x), v_w\right)$ (stretching, suction/injection) velocity, c dimensional constants, h_s wall convective heat transfer coefficient , Λ_2 concentration expansion coefficient, C liquid concentration**,** h_c wall(sheet) convective mass transfer coefficient, C_∞ ambient concentration liquid**,** and u, v are the elements of fluid velocity in the x, y direction respectively. Implementing suitable similarity transformations [29]:

$$\begin{cases}\eta=y\sqrt{\frac{a}{\nu}},\ u=axf'\left(\eta\right),\ v=-\sqrt{a\nu}\,f\left(\eta\right),\\ \theta(\eta)=\frac{T-T_\infty}{T_f-T_\infty}, \phi(\eta)=\frac{C-C_\infty}{C_f-C_\infty}.\end{cases} \quad \textbf{(7)}$$

The continuity equation (i.e., Eq. (1)) is satisfied via the Cauchy-Riemann equations, and the momentum, energy (heat) and concentration equations in dimensionless form emerge as:

$$f''' + f\, f'' + \beta_1\left(2f\, f'\, f'' - f^2 f'''\right) + \beta_2\left(f''^2 - ff^{(iv)}\right) - \left(f'\right)^2 \\ + \delta\left[\left(1+\beta_t\theta\right)\theta + N\left(1+\beta_c\phi\right)\phi\right] + A^2 = 0, \tag{8}$$

$$\left(1+R\right)\theta'' + \frac{4}{3}R\begin{bmatrix} \left(\theta_R - 1\right)^3\left(3\theta^2\left(\theta'\right)^2 + \theta^3\theta''\right) \\ +3\left(\theta_R - 1\right)^2\left(2\theta\left(\theta'\right)^2 + \theta^2\theta''\right) \\ +3\left(\theta_R - 1\right)\left(\left(\theta'\right)^2 + \theta\theta''\right) \end{bmatrix} \\ + \Pr f\theta' + \Pr\left(N_t\theta'^2 + N_b\phi'\theta'\right) = 0, \tag{9}$$

$$\phi'' + Sc\left(f\phi' - \gamma\phi\right) + \frac{N_t}{N_b}\theta'' = 0, \tag{10}$$

$$\begin{cases} \text{at}\,\eta = 0,\ f = S,\ f' = 1,\ \phi = -\gamma_2\left(1-\phi\left(\eta\right)\right),\ \theta = -\gamma_1\left(1-\theta\left(\eta\right)\right), \\ \qquad \text{as}\ \ \eta\to\infty,\ f'\to A,\ \phi\to 0,\ \theta\to 0\,. \end{cases} \tag{11}$$

Here $\left(\,'\,\right)$ signifies differentiation concerning η, λ the mixed convection parameter, Sc the Schmidt number, Gr_x the thermal buoyancy number, β_1 the dimensionless relaxation time parameter, $\sigma < 0$ the generative reaction variable, Gr_x^* the concentration buoyancy number, β_2 the dimensionless retardation time parameter, β_t the nonlinear thermal convection parameter, N_t the thermophoresis parameter, θ_R the temperature ratio parameter β_c the nonlinear concentration convection parameter, $\Pr$ the Prandtl number, N_b the Brownian motion parameter, R the radiation variable, A the ratio of rates, γ_1 the thermal Biot number, N the buoyancy ratio parameter, γ_2 the concentration Biot number, $\sigma > 0$ the destructive reaction variable and $(S > 0)$ the suction and $(S < 0)$ the injection. These parameters are defined as follows:

$$\begin{gathered} \beta_1 = c\lambda_1, \beta_2 = c\lambda_2,\ \delta = \frac{Gr_x}{\mathrm{Re}_x^2},\ Gr_x = \frac{g\Lambda_1 T_\infty x^3}{\nu^2},\ \mathrm{Gr}_x^* = \frac{g\Lambda_3 C_\infty x^3}{\nu^2}, \\ \beta_t = \frac{\Lambda_2 T_\infty}{\Lambda_1},\ \beta_c = \frac{\Lambda_4 C_\infty}{\Lambda_3},\ N = \frac{Gr_x^*}{Gr_x},\ \mathrm{Re}_x = \frac{xu_w}{\nu},\ S = \frac{v_w}{\sqrt{c\nu}} \\ N_t = \frac{\tau D_T}{T_\infty \nu},\ A = \frac{e}{c},\ \Pr = \frac{\nu}{\alpha},\ N_b = \frac{\tau D_B}{\nu}, \gamma = \frac{K_1}{c}, \theta_R = \frac{T_f}{T_\infty}, \\ R = \frac{4\sigma^* T_\infty^3}{kk^*},\ Sc = \frac{\nu}{D_B},\ \gamma_1 = h_s\sqrt{\frac{\nu}{c}},\ \gamma_2 = h_c\sqrt{\frac{\nu}{c}}. \end{gathered} \tag{12}$$

Expressions for local Nusselt and local Sherwood numbers are:

$$Nu_x = -\frac{xq_w}{k\left(T - T_\infty\right)},\ q_w = -\left(k + \frac{16\sigma^* T_\infty^3}{3k^*}\right)\left(\frac{\partial T}{\partial y}\right)_{y=0}, \tag{13}$$

$$Sh_x = -\frac{xj_w}{D_B\left(C - C_\infty\right)},\ j_w = -D_B\left(\frac{\partial C}{\partial y}\right)_{y=0}. \tag{14}$$

In non–dimensional form, one has:

$$Nu_x Re_x^{-0.5} = -\left(1 + \frac{4}{3} R\left(\theta_R\right)^3\right)\theta'(0) \tag{15}$$

$$Sh_x Re_x^{-0.5} = -\phi'(0) \tag{16}$$

3. Analytical solution procedure

Here, convergent series solutions of the nonlinear ordinary differential equations (8) to (10) along with boundary conditions (11) are obtained using the homotopy analysis scheme [48]. This is a semi-numerical rapidly convergent procedure which provides exceptionally high accuracy for nonlinear ordinary or partial differential equation systems which are common in robotic smart nanopolymer coating fluid mechanics. For the problem under consideration, the required initial estimations $\left(f_o(\eta),\ \theta_o(\eta),\ \phi_o(\eta)\right)$ and essential linear operators $\left(L_f,\ L_\theta,\ L_\phi\right)$ are specified as:

$$\left.\begin{aligned} f_0(\eta) &= S + A*\eta + (1-A)\left(1-e^{-\eta}\right), \\ \theta_0(\eta) &= \left(\frac{\gamma_1}{1+\gamma_1}\right)*e^{-\eta}, \\ \phi_0(\eta) &= \left(\frac{\gamma_2}{1+\gamma_2}\right)*e^{-\eta}, \end{aligned}\right\} \tag{17}$$

$$\left.\begin{cases} L_f = f''' - f', \\ L_\theta = \theta'' - \theta, \\ L_\phi = \phi'' - \phi, \end{cases}\right\} \tag{18}$$

With:

$$\left.\begin{cases} L_f\left(A_1 + A_2 e^{\eta} + A_3 e^{-\eta}\right) = 0, \\ L_\theta\left(A_4 e^{\eta} + A_5 e^{-\eta}\right) = 0, \\ L_\phi\left(A_6 e^{\eta} + A_7 e^{-\eta}\right) = 0, \end{cases}\right\} \tag{19}$$

Here $C_i\left(i=1-7\right)$ indicate the arbitrary constants.

4. Convergence analysis for HAM

The homotopic algorithm encompasses auxiliary parameters h_f, h_θ and h_ϕ which efficiently control the convergence region of homotopic solutions. These parameters (h_f, h_θ and h_ϕ) are evaluated via plotting h-curves [**See Fig. 2**].

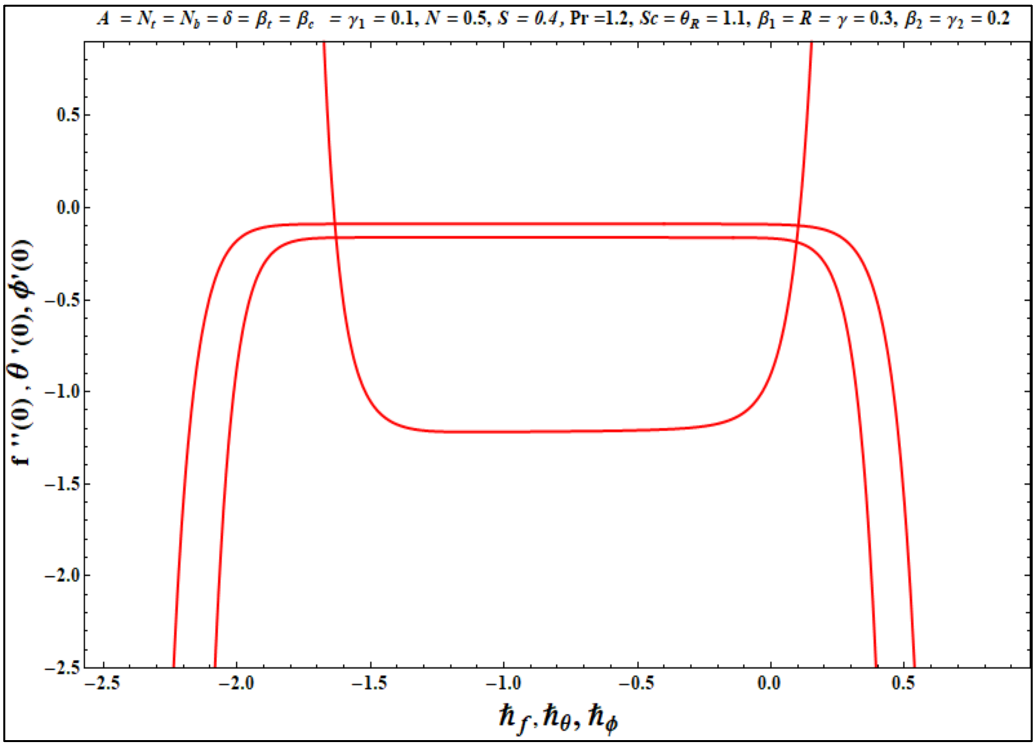

Figure 2. –curve against on $f''(0)$, $\theta'(0)$ and $\phi'(0)$.

From **Fig. 2** we obtain $-1.2 \le h_f \le -0.4$, $-1.2 \le h_\theta \le -0.2$ and $-1.2 \le h_\phi \le -0.2$, respectively.

Table 1. Assessment of convergence series solutions for the various order of approximations when $\gamma_1 = A = \delta = N_t = N_b = \beta_t = \beta_c = 0.1$, $N = 0.5$, $S = 0.4$, $\Pr = 1.2$, $\theta_R = Sc = 1.1$, $R = \beta_1 = \gamma = 0.3$ and $\beta_2 = \gamma_2 = 0.2$.

Order of approximations	$-f''(0)$	$-\theta'(0)$	$-\phi'(0)$
1	1.0659	0.08967	0.1630
5	1.1889	0.08879	0.1625
10	1.2078	0.08868	0.1622
15	1.2136	0.08866	0.1621
20	1.2164	0.08867	0.1620
25	1.2187	0.08867	0.1620
30	1.2187	0.08867	0.1620
35	1.2187	0.08867	0.1620

Table 1 shows the convergence of homotopic solutions for velocity $f''(0)$, temperature $\theta'(0)$ and nanoparticle species concentration $\phi'(0)$. It is revealed that the 25th order of approximation is sufficient for velocity, whereas temperature and concentration require only the 20th order of approximations.

5. Comparison of HAM results

Tables 2 and 3 shows the benchmarking of HAM solutions for coating skin friction $-C_{fx}\,\mathrm{Re}_x^{-\frac{1}{2}}$ with earlier simpler models [31, 32] and [49, 50]. An excellent agreement has been attained with the current homotopy solutions as testified to in these tables confirming the validity and accuracy of the present analytical results.

Table 2. Comparison results of $f''(0)$ for β_1 when $A = \delta = 0$.

β_1	Ref. [31]	Ref. [32]	Present study
0.0	-1.000000	-1.000000	-1.000000
0.2	-1.051889	-1.051838	-1.051901
0.4	-1.1019032	-1.101842	-1.101841
0.6	-1.1501373	-1.150231	-1.150231
0.8	-1.1967113	-1.197532	-1.196711
1.2	-1.2853632	-1.285317	-1.285316

Table 3. Comparison results of $f''(0)$ for β_2 when $A = \delta = 0$ with fixed $\beta_1 = 0.4$.

β_2	Ref. [49]	Ref. [50]	Present study
0.0	1.10190	1.10193	1.10193
0.2	1.00498	1.00493	1.00493
0.4	0.92986	0.92975	0.92975
0.6	0.86942	0.86654	0.86654
0.8	0.81943	0.81932	0.81932
1.0	0.77718	0.77681	0.77681

6. Results and discussion

This section captures the significance of involved parameters against dimensionless concentration, temperature and velocity profiles via **Figs. 3-19 and Table 4**. The values of parameters are considered in the ranges as follows:

$A\,(0.2 \le A \le 1.6)$ $\beta_1\,(0.2 \le \beta_1 \le 0.8)$, $\beta_2\,(0.2 \le \beta_2 \le 0.8)$, $\delta\,(1.0 \le \delta \le 7.0)$, N ($10.0 \le N \le 40.0$), $S\,(-0.5 \le S \le 0.5)$,

$\Pr\,(0.1 \le \Pr \le 0.7)$, $N_t\,(1.0 \le N_t \le 4.0)$, $R\,(0.1 \le R \le 0.7)$, $N_b\,(1.0 \le N_b \le 4.0)$, θ_R ($1.0 \le \theta_R \le 2.5$), $\gamma_1\,(0.1 \le \gamma_1 \le 0.4)$, $Sc\,(0.1 \le Sc \le 0.7)$, $N_b\,(0.1 \le N_b \le 0.4)$, N_t ($0.1 \le N_t \le 0.4$), $\gamma\,(-0.3 \le \gamma \le 0.3)$ and γ_2 $(0.1 \le \gamma_2 \le 0.4)$.

6.1 Velocity Profile

Figs. 3-9 disclose the impact of A, β_1 β_2, δ S and N on velocity $f'(\eta)$. Fig. 3. demonstrates that an increment in the velocity ratio factor A, $f'(\eta)$ indicates an improvement with respect to η in the boundary regime, that is, the fluid motion is accelerated on the stretchy surface. When $(A > 1)$ free stream velocity is stronger than the stretching velocity of the surface, this builds a momentum upsurge in the flow domain through exterior free stream which exhibits high acceleration for all horizontal coordinate values, η. Consequently, the thickness of the momentum boundary layer of the stretching surface is therefore decreased. This has an influence on the quality control of manufactured coatings. However, when $(A < 1)$ the stretching velocity of the sheet is higher than the exterior velocity of free stream and the reverse impact is calculated. i.e., velocity of Oldroyd-B fluid $f'(\eta)$ is decreased and thickness of momentum boundary layer on the surface increases. If $(A = 1)$ both the external and the stretching velocity of the Oldroyd-B fluid are identical. This scenario is a natural intermediate between cases where A > 1 and A< 1. It is evident that higher stretching sheet prevents the development of momentum; however, a stronger external velocity of corresponding Oldroyd-B fluid is produced. The influence of Deborah numbers on the velocity of Oldroyd-B fluid $f'(\eta)$ that is in terms of (β_1 relaxation time quantity) and (β_2 retardation time quantity) are portrayed in Fig. 4 and 5. respectively. Here in Fig. 4, it is clear that as (relaxation time fluid) β_1 rises, the Oldroyd-B fluid velocity gradually declines. In fact, β_1 is mathematically expressed as ‘‘the ratio of the observational timescale to the time scale of the material reaction”. We can examine the three different scenarios to assess the polymeric behavior of materials. (i) When $(\beta_1 = 1)$ for viscoelastic substance, (ii) when $(\beta_1 << 1)$ for entirely viscous material, (iii) when $(\beta_1 >> 1)$ for elastic material in nature. Higher values of β_1 lead to a lower relaxation relative to the characteristic timescale. This means that fluid react in a similar way to solid materials. Fig. 5 displays the impact of retardation time $(\beta_2 = 0.2,\ 0.4,\ 0.6,\ 0.8)$ parameter on Oldroyd-B fluid velocity $f'(\eta)$. As anticipated, $f'(\eta)$ upsurges when β_2 is increased. Physically, retardation time augments for increasing β_2 owing to which $f'(\eta)$ upsurges. Fig. 6 reveals the features of mixed convection variable δ on $f'(\eta)$. Clearly $f'(\eta)$ increases when the mixed convection variable is elevated. Since thermal buoyancy forces exceed the viscous forces with higher values of δ, this intensifies the flow. Fig. 7 unveils the impact of buoyancy ratio variable N on $f'(\eta)$. It can be seen that a massive boost is induced in the linear velocity across the domain with stronger values of $N = \frac{Gr_x^*}{Gr_x}$. Note that $N >> 1$ signifies that the concentration buoyancy force Gr_x^* of nanoparticles is much stronger than the temperature buoyancy force Gr_x. Consequently, the hydrodynamic boundary layer thickness of Oldroyd-B fluid increases. Fig. 8 depicts the characteristics of wall suction/injection on $f'(\eta)$. It is analyzed that the impetus of linear velocity is increased with amplification in the injection parameter $(S < 0)$. On the other hand, it is decreased for greater values of wall suction factor $(S > 0)$. It is evident that injection of nanofluid augments momentum development in the boundary layer regime and, consequently, velocity of Oldroyd-B nanofluid increases. This effect is also known as blowing in manufacturing processes. The reverse situation is noticed for suction which causes the boundary layer to adhere more strongly to the wall and decelerates flow- this increases momentum boundary layer thickness.

6.2. Temperature Profile

Figs.9–14 display the effect of R, Pr, γ_1 N_t, θ_R and N_b on $\theta(\eta)$. Fig. 9 depicts the $\theta(\eta)$ curves subjected to Prandtl number $(\Pr)$ values. This Fig. exhibits that the nanofluid temperature decreases for larger Prandtl number. Prandtl number ($\Pr$) communicates the rate of momentum to thermal diffusion. Liquid conductivity retards for larger $\Pr$. The heat transferred via conduction of molecules is subsequently repressed which expresses a decay in $\theta(\eta)$ and a diminution in thickness of thermal boundary-layer. Chilling of stretched coating system is thus attained with increasing $\Pr$ while heating is witnessed with lower $\Pr$. Fig. 10 illustrates the curves of $\theta(\eta)$ under the impact of R. It is witnessed that when R is increased, $\theta(\eta)$ is obviously enhanced. Actually, greater heat (thermal energy) is produced in the working liquid during the radiation process (i.e., for higher R values), causing the temperature of the nanofluid in the boundary layer regime to increase. Fig. 11 divulges the consequence of Buongiorno's model parameter (nanoscale thermophoresis N_t) on thermal distribution $\theta(\eta)$ of Oldroyd-B fluid. Stronger movement of nanoparticles in the stagnation boundary layer flow domain is encouraged by the thermophoretic body force; nanoparticles are mobilized from the hotter region to the cooler one and therefore higher thermal transmission arises in the flow field. Hence, intensifying magnitude of nanoscale thermophoresis parameter N_t produces substantial thermal diffusion enhancement and boosts temperature and thermal boundary layer thickness. The influence of the Brownian motion factor N_b on the temperature $\theta(\eta)$ of the Oldroyd-B nanofluid are presented in Fig. 12. There is an accentuation in nanofluid temperature $\theta(\eta)$ and also thermal boundary-layer thickness with increment in N_b. In fact, the random movement of the fluid particles is increased since nanoparticle diameters are reduced with higher Brownian motion parameter and this generates intensification in ballistic collisions which produces extra heat in the regime. Micro-convection around the nanoparticles is also enhanced with greater Brownian motion effects. All these factors contribute to marked thermal enhancement. The effect of temperature ratio variable θ_R on temperature distribution $\theta(\eta)$ is illustrated in Fig. 13. Physically, temperature appears to rise significantly as θ_R increases. Higher values of θ_R implies an elevation in wall temperature which makes the depth of thermal penetration deeper into the boundary layer. Heat transfer into the flow from the wall is therefore encouraged. Also, when the liquid temperature T_f exceeds the ambient temperature T_∞ (in energy equation) this creates a larger temperature differential across the boundary layer which intensifies thermal diffusion from the wall to the free stream and manifests in a boost in $\theta(\eta)$ rises. Fig. 14 shows that with larger values of thermal Biot number γ_1 , there is an improvement in the temperature field $\theta(\eta)$. The condition $\gamma_1 = 0$ suggests the configuration of isoflux at the wall, while $\gamma_1 \to \infty$ symbolizes the configuration of an isothermal wall. In addition, this parameter is featured in the prescribed boundary condition $\theta = -\gamma_1(1-\theta(\eta))$ (from Eqn. (11)) which determines the intensity of Biot number. Therefore, stronger values of Biot number γ_1 corresponds to an amplification in thermal convection over the stretching sheet which enhances the nanofluid temperature. The inclusion of this complex convective wall boundary condition provides a more realistic estimation of manufacturing conditions than conventional boundary conditions.

6.3. Concentration Profile

Figs.15–19 show the impact of Sc, γ, N_t, γ_2, and N_b on $\phi(\eta)$. Fig. 15 reveals that with higher values of Sc, the nanoparticle concentration $\phi(\eta)$ and thickness of solutal boundary-layer reduces. Actually, Schmidt number is the ratio of momentum to the nanoparticle molecular diffusivity which implies that when Sc rises, mass diffusivity reduces and there is a depletion in concentration $\phi(\eta)$. The judicious selection of nanoparticles to embed in the coating regime is therefore critical in achieving bespoke mass transfer characteristics in fabrication processes. Figs. 16 and 17 portray the evolution in concentration $\phi(\eta)$ of nanoparticles with different values of thermophoresis N_t and Brownian N_b diffusion parameters. When N_b increases, an increasing trend is seen via higher chaotic movement associated with higher N_b, the particle collision is boosted, and mass diffusion is assisted. As a result, the Oldroyd-B nanofluid concentration upsurges. The reverse trend is noted for the influence of thermophoresis parameter N_t on the surface concentration $\phi(\eta)$. Physically, the movement of nanoparticles from the wall to the interior boundary layer region is impeded by an elevation in the thermophoretic force. Therefore, this factor leads to reduction of $\phi(\eta)$ i. e.

mass diffusion into the boundary layer is suppressed. Fig. 18 displays that with increasing values of mass transfer Biot number γ_2 , there is an enhancement in magnitudes of the concentration field $\phi(\eta)$. This key parameter appears in the relevant boundary conditions of concentration. i.e. $\phi = -\gamma_2\left(1-\phi(\eta)\right)$. Greater values of γ_2 significantly boost the concentration of nanoparticles but decrease the gradient of concentration at the wall sequentially. In Fig. 19, it is evident that higher values of destructive parameter $\gamma > 0$, the concentration profile of Oldroyd-B nanofluid exhibits a diminishing trend. With larger values of generative parameter $\gamma < 0$, the concentration of nanoparticles increases. Practically, it is found that when the reaction rate in the fluid is increased, then greater conversion of the original nanoparticle species is induced in the presence of chemical reaction and thus the concentration of the original nanoparticles reduces. On the other hand, when the reaction rate in the liquid is decreased then less original species is converted and nanoparticle concentration values are increased.

The numerical findings for $Nu_x \operatorname{Re}_x^{-\frac{1}{2}}$ and $Sh_x \operatorname{Re}_x^{-\frac{1}{2}}$ for diverse values of β_1, β_2, θ_R, γ, N_t and N_b are disclosed in **Table. 4**. Here it is examined that, the heat and mass transfer rates suppressed for the growing values of relaxation β_1 and retardation β_2 fluid parameters, respectively. Since the stronger values of β_1 and β_2 upsurge the relaxation and retardation times parameters of Oldroyd-B liquid, this induces a reduction in rate of heat and mass transfer at the wall. The heat and mass transfer rates are boosted for greater values of θ_R. When the liquid temperature T_f is greater than the ambient temperature T_∞ this effectively increases the thermal conductivity of nanofluid, as θ_R increases. Heat transfer to the wall is therefore enhanced. Moreover, the chemical reaction variable γ increasing suppresses concentration and temperature magnitudes in the boundary layer but elevates transport of nanoparticles and heat to the wall. $Nu_x \operatorname{Re}_x^{-\frac{1}{2}}$ and $Sh_x \operatorname{Re}_x^{-\frac{1}{2}}$ are therefore increased. It is also apparent that heat and mass transfer rates are suppressed with increasing values of Brownian and thermophoretic parameters. This is consistent with the results described earlier wherein temperatures and nanoparticle concentrations were boosted with these parameters. This leads to a depletion in the migration of heat and nanoparticle species to the wall away from the boundary layer and explains the plummet in local Nusselt and Sherwood number functions with higher Brownian motion and thermophoresis parameters. Again, the prescription of appropriate nanoparticles is critical in developing the desired nano-coating properties for delicate micro-machining applications since heat, mass and momentum characteristics are strongly influenced by for example nanoparticle mass diffusivity, nanoparticle thermal conductivity and also the nanofluid viscosity which is a function of the nanoparticle concentration.

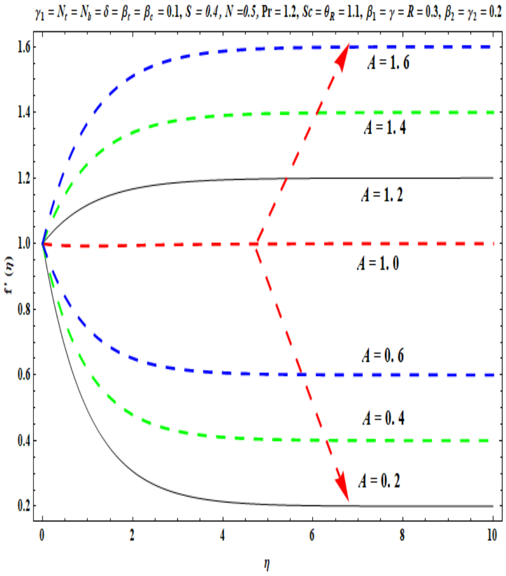

Figure 3. against A.

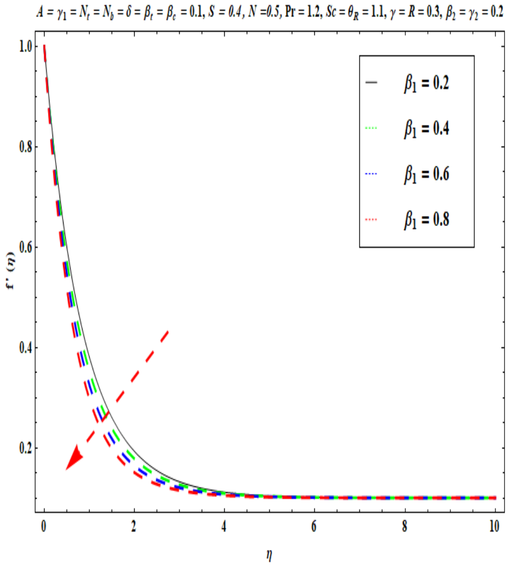

Figure 4. $f'(\eta)$ against β_1.

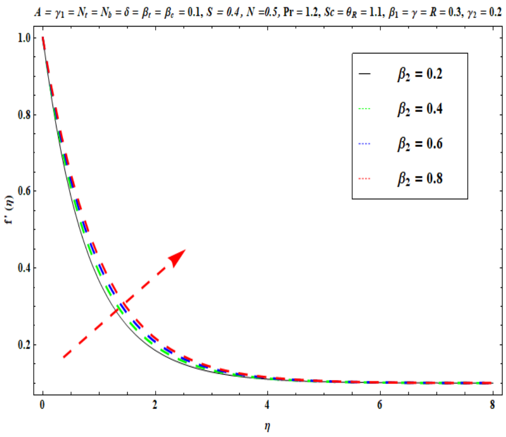

Figure 5. $f'(\eta)$ against β_2..

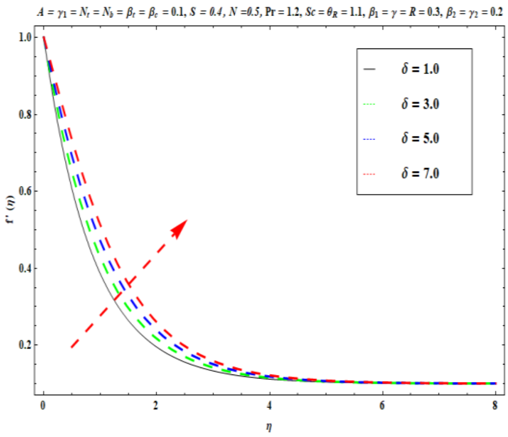

Figure 6. $f'(\eta)$ against δ.

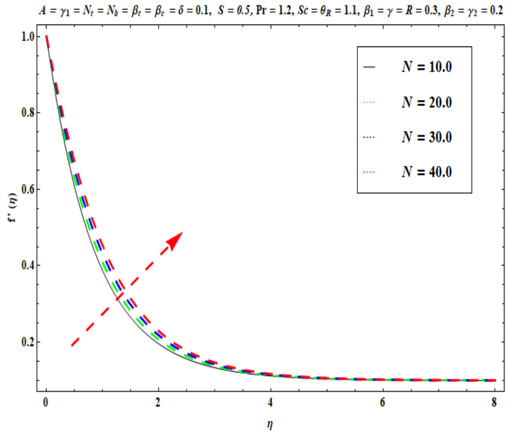

Figure 7. $f'(\eta)$ against N.

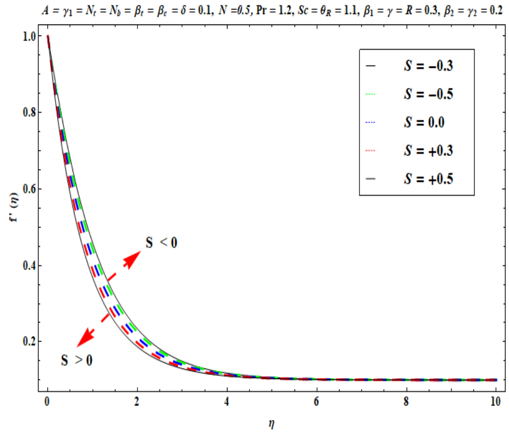

Figure 8. $f'(\eta)$ against S.

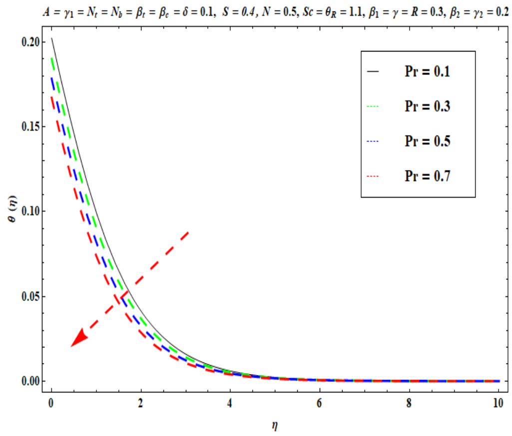

Figure 9. $\theta(\eta)$ against Pr.

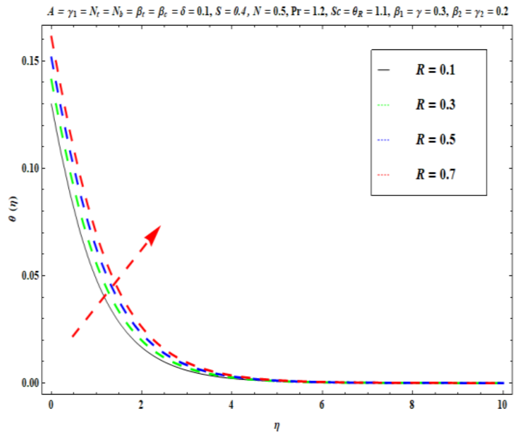

Figure 10. $\theta(\eta)$ against R.

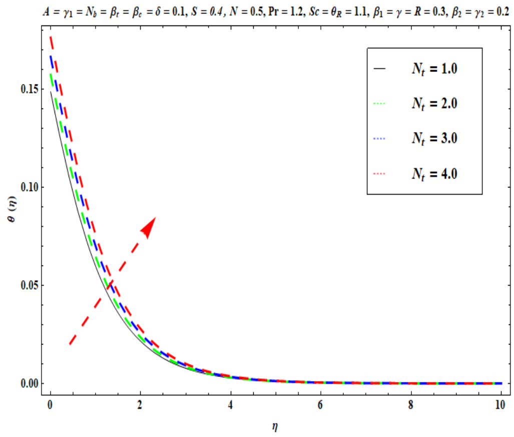

Figure 11. $\theta(\eta)$ against N_t.

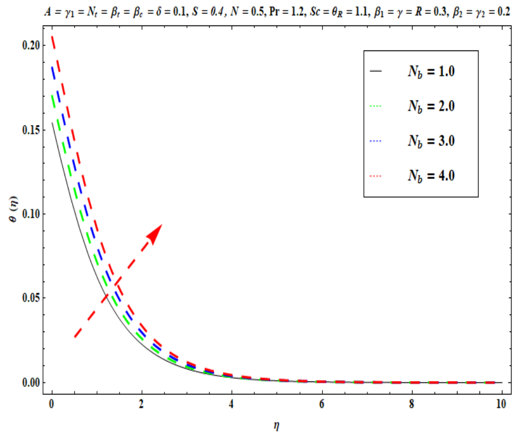

Figure 12. $\theta(\eta)$ against N_b.

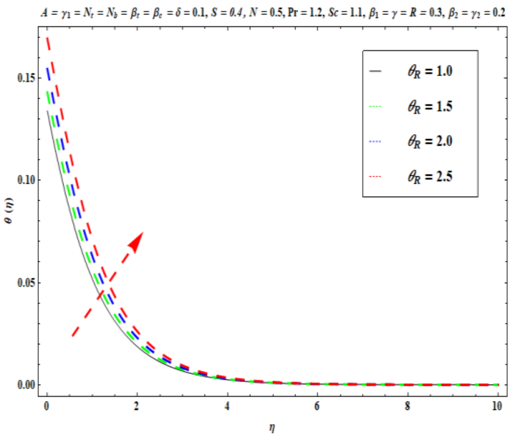

Figure 13. $\theta(\eta)$ against θ_R.

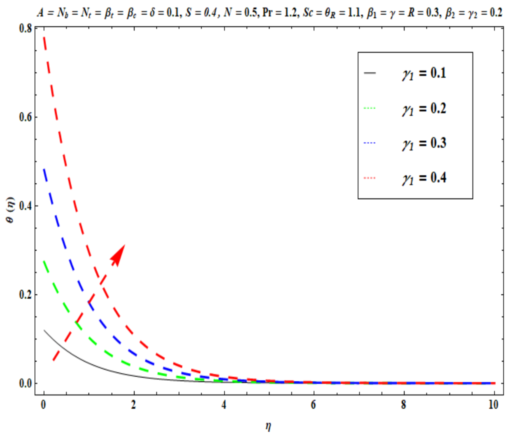

Figure 14. $\theta(\eta)$ against γ_1.

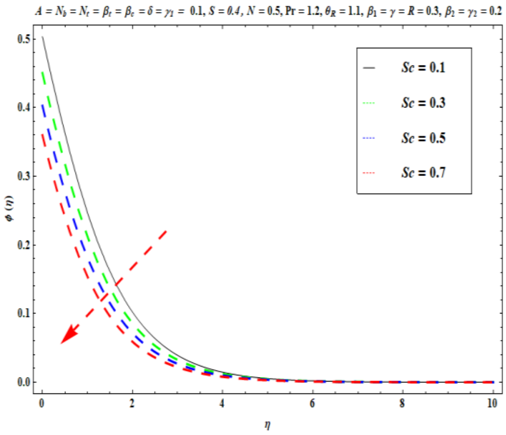

Figure 15. $\phi(\eta)$ against Sc.

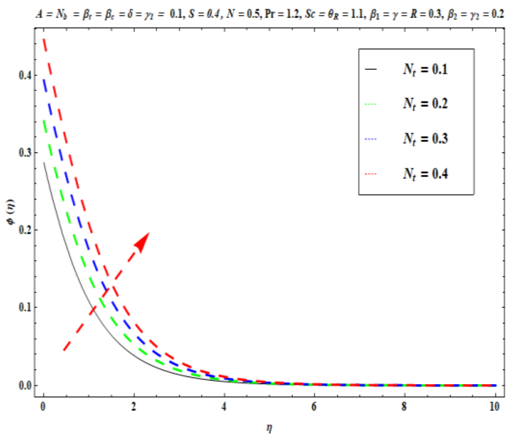

Figure 16. $\phi(\eta)$ against N_t.

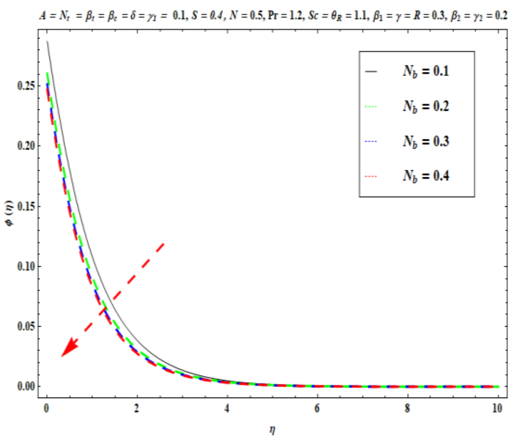

Figure 17. $\phi(\eta)$ against N_b.

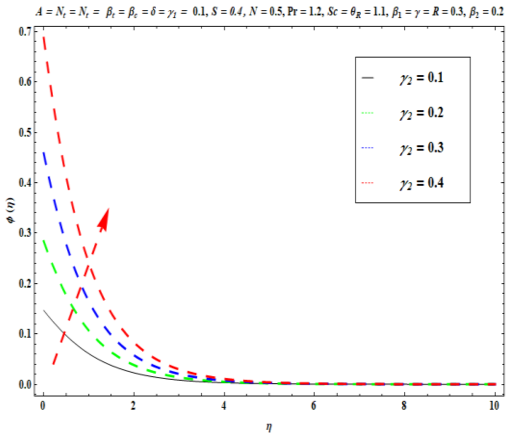

Figure 18. $\phi(\eta)$ against γ_2.

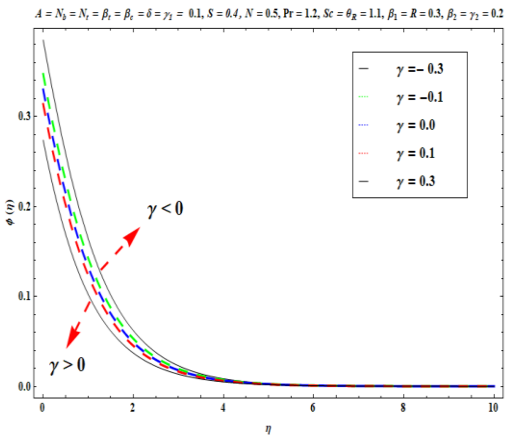

Figure 19. $\phi(\eta)$ against γ.

Table 4. Numerical values of $Nu_x \mathrm{Re}_x^{-\frac{1}{2}}$ and $Sh_x \mathrm{Re}_x^{-\frac{1}{2}}$ considering $A<1$.

β_1	β_2	θ_R	γ	N_t	N_b	$Nu_x \mathrm{Re}_x^{-\frac{1}{2}}$	$Sh_x \mathrm{Re}_x^{-\frac{1}{2}}$
0.1	0.1	1.1	0.3	0.1	0.1	0.1360	0.1623
0.2						0.1359	0.1621
0.3						0.1358	0.1619
0.1	0.2					0.1361	0.1624
	0.3					0.1362	0.1625
	0.4					0.1363	0.1626
	0.1	1.2				0.1499	0.1624
		1.3				0.1662	0.1625
		1.4				0.1852	0.1626
		1.1	0.4			0.1360	0.1642
			0.5			0.1361	0.1659
			0.6			0.1362	0.1674
			0.3	0.2		0.1359	0.1546
				0.3		0.1358	0.1469
				0.4		0.1357	0.1422
				0.1	0.2	0.1359	0.1564
					0.3	0.1358	0.1453
					0.4	0.1357	0.1413

7. Closing remarks

Inspired by analyzing more rigorously the stagnation-flow coating regimes in micro-machine and robotic manufacturing, the current article has developed a novel mathematical model for nonlinear mixed convection flow of Oldroyd-B type nanoliquid subjected to a chemical reaction from the stretching surface. The impacts of thermophoresis along with Brownian motion features induced by nanoparticles are investigated using Buongiorno's nanoscale model. High-temperature heat transfer is evaluated considering a nonlinear version of thermal radiation. The consistent momentum, energy, and nanoparticles volume fraction equations are altered into a set of nonlinear ordinary differential ones and then solved analytically utilizing the homotopy algorithm. Comparison of HAM results with earlier studies are included. The assessment of convergent series solutions is also presented. The main findings emerging from the elaborated analysis are summarized below:

- Influences of fluid relaxation and retardation times parameters are qualitatively opposite for the velocity profile of the Oldroyd-B nanoliquid (coating).
- Increment in mixed convection parameter improves the velocity profile.
- Temperature and nanoparticles concentration show an increasing trend for higher values of thermophoresis parameter.
- A rise in temperature ratio parameter leads to higher temperature magnitudes.
- Stronger values of thermal and solutal Biot numbers cause an augmentation in fluid temperature and concentration of nanoparticles.
- An enhancement in Brownian motion transfers kinetic energy to heat energy, which increases the temperature of the nanofluid and elevates thermal boundary layer thickness.
- The current Oldroyd-B viscoelastic nanofluid model reduces to the classical viscous fluid case when $\beta_1 = \beta_2 = 0$. Important thermal, hydrodynamic and species transport characteristics can be captured with the Oldroyd-B viscoelastic formulation presented which are not possible with classical Newtonian or simpler non-Newtonian models. The results presented are more realistic for actual nano-polymeric coating processes in robotics, sensor and micromachine surface deposition technologies.

The current study provides a good platform for further research in high temperature nano-polymeric coating flow processes. It has however neglected certain aspects including *consideration of variable sheet thickness, activation energy, Joule heating, entropy generation, Cattaneo-Christov heat-mass fluxes and bio-convective flows with gyrotactic microorganisms*. These may be explored imminently.

Conflict of interest:

The authors have no conflict of interest related to this manuscript.

References

1]. Sakiadis, B. C. (1961). Boundary-layer behavior on continuous solid surfaces: I. Boundary-layer equations for two-dimensional and axisymmetric flow. *AIChemE Journal*, *7*(1), 26-28.

2]. Crane, L. J. (1970). Flow past a stretching plate. *Zeitschrift für angewandte Mathematik und Physik ZAMP*, *21*(4), 645-647.

3]. Govindaraj, N., Singh, A. K., Roy, S., & Shukla, P. (2019). Analysis of a boundary layer flow over moving an exponentially stretching surface with variable viscosity and Prandtl number. *Heat Transfer—Asian Research*, *48*(7), 2736-2751.

4]. Ibrahim, W., & Gadisa, G. (2020). Nonlinear convective boundary layer flow of micropolar-couple stress nanofluids past permeable stretching sheet using Cattaneo-Christov heat and mass flux model. *Heat Transfer*, *49*(5), 2521-2550.

5]. Rajput, G. R., Jadhav, B. P., & Salunkhe, S. N. (2020). Magnetohydrodynamics boundary layer flow and heat transfer in porous medium past an exponentially stretching sheet under the influence of radiation. *Heat Transfer*, *49*(5), 2906-2920.

6]. Eldabe, N. T., Gabr, M. E., Zaher, A. Z., & Zaher, S. A. (2021). The effect of Joule heating and viscous dissipation on the boundary layer flow of a magnetohydrodynamics micropolar-nanofluid over a stretching vertical Riga plate. *Heat Transfer*, *50*(5), 4788-4805.

7]. Dawar, A., Shah, Z., Tassaddiq, A., Islam, S., & Kumam, P. (2021). Joule heating in magnetohydrodynamic micropolar boundary layer flow past a stretching sheet with chemical reaction and microstructural slip. *Case Studies in Thermal Engineering*, *25*, 100870.

8]. Nadeem, S., Fuzhang, W., Alharbi, F. M., Sajid, F., Abbas, N., El-Shafay, A. S., & Al-Mubaddel, F. S. (2022). Numerical computations for Buongiorno nano fluid model on the boundary layer flow of viscoelastic fluid towards a nonlinear stretching sheet. *Alexandria Engineering Journal*, *61*(2), 1769-1778.

9]. M. Nasir, M. Waqas, **O. Anwar Bég**, N. Zamri, H. J. Leonard and K. Guedri, Dynamics of tangent-hyperbolic nanoliquids configured by stratified extending surface: Effects of transpiration, Robin conditions and dual stratifications, *International Communications in Heat and Mass Transfer*, 139 (2022) 106372.

10]. M. Waqas, M. A. Sadiq and H. M. S. Bahaidarah, Gyrotactic bioconvection stratified flow of magnetized micropolar nanoliquid configured by stretchable radiating surface with Joule heating and viscous dissipation, *International Communications in Heat and Mass Transfer* 138 (2022) 106229.

11]. M. Nasir, M. Waqas, N. Zamri, K. Guedri and A. M. Galal, Modeling and analytical analysis of dual diffusive Williamson nanoliquid considering generalized heat-mass concepts, *International Journal of Modern Physics B* (2022) https://doi.org/10.1142/S021797922350056X.

12]. M. Waqas, W. A.Khan, A. A. Pasha, N. Islam and M. M. Rahman, Dynamics of bioconvective Casson nanoliquid from a moving surface capturing gyrotactic microorganisms, magnetohydrodynamics and stratifications, *Thermal Science and Engineering Progress* (2022). doi.org/10.1016/j.tsep.2022.101492.

13]. M. Nasir, M. Waqas, N. Zamri, M. Jameel, K. Guedri and A. M. Galal, Rheology of tangent-hyperbolic (T-H) nanoliquid configured by stretchable stratified surface considering transpiration effects, *International Journal of Modern Physics B* (2022) https://doi.org/10.1142/S0217979223500571.

14]. N. Abbas, K. U. Rehman, W. Shatanawi and K. Abodayeh, Mathematical model of temperature-dependent flow of power-law nanofluid over a variable stretching Riga sheet, *Waves in Random and Complex Media* (2022) https://doi.org/10.1080/17455030.2022.2111029.

15]. M. Nasir, M. Waqas, M. S. Kausar, **O. Anwar Bég** and N. Zamri, Cattaneo-Christov dual diffusive non-Newtonian nanoliquid flow featuring nonlinear convection, *Chinese Journal of Physics* (2022). https://doi.org/10.1016/j.cjph.2022.05.005.

16]. Abbasi, A., Farooq, W., Tag-ElDin, E. S. M., Khan, S. U., Khan, M. I., Guedri, K. & Galal, A. M. (2022). Heat transport exploration for hybrid nanoparticle (Cu, Fe3O4)—based blood flow via tapered complex wavy curved channel with slip features. *Micromachines*, *13*(9), 1415.

17]. Waqas, H., Oreijah, M., Guedri, K., Khan, S. U., Yang, S., Yasmin, S., & Galal, A. M. (2022). Gyrotactic motile micro-organisms impact on pseudoplastic nanofluid flow over a moving Riga surface with exponential heat flux. *Crystals*, *12*(9), 1308.

18]. Ahmed, M. F., Zaib, A., Ali, F., Bafakeeh, O. T., Tag-ElDin, E. S. M., Guedri, K. & Khan, M. I. (2022). Numerical computation for gyrotactic microorganisms in Mhd radiative Eyring–Powell nanomaterial flow by a static/moving wedge with Darcy–Forchheimer relation. *Micromachines*, *13*(10), 1768.

19]. Zahoor Raja, M. A., Shoaib, M., Tabassum, R., Khan, M. I., Jagannatha, C. G., & Gali, C. (2022). Performance analysis of backpropagated networks for entropy optimized mixed convection nanofluid with second-order slip over a stretching surface. *Waves in Random and Complex Media*, 1-23.

20]. Chu, Y. M., Khan, M. I., Abbas, T., Sidi, M. O., Alharbi, K. A. M., Alqsair, U. F., ... & Malik, M. Y. (2022). Radiative thermal analysis for four types of hybrid nanoparticles subject to non-uniform heat source: Keller box numerical approach. *Case Studies in Thermal Engineering*, *40*, 102474.

21]. Gendy, M. E., **O. Anwar Bég**, Kadir, A., Islam, M. N., & Tripathi, D. (2021). Computational fluid dynamics simulation and visualization of Newtonian and non-Newtonian transport in a peristaltic micro-pump. *Journal of Mechanics in Medicine and Biology*, *21*(08), 2150058.

22]. Trujillo-de Santiago, G., Rojas-de Gante, C., Garcıa-Lara, S., Ballescá-Estrada, A., & Alvarez, M. M. (2014). Studying Mixing in Non-Newtonian Blue Maize Flour, *PLoS ONE* 9(11): e112954.

23]. Maingonnat, J. F., Doublier, J. L., Lefebvre, J., & Delaplace, G. (2008). Power consumption of a double ribbon impeller with Newtonian and shear thinning fluids and during the gelation of an iota-carrageenan solution. *Journal of Food Engineering*, *87*(1), 82-90.

24]. Syrjälä, S. (1995). Finite-element analysis of fully developed laminar flow of power-law non-Newtonian fluid in a rectangular duct. *International communications in heat and mass transfer*, *22*(4), 549-557.

25]. Siginer, D. A., & Letelier, M. F. (2010). Heat transfer asymptote in laminar flow of non-linear viscoelastic fluids in straight non-circular tubes. *International journal of engineering science*, *48*(11), 1544-1562.

26]. Akbar, N. S., Tripathi, D., **O. Anwar Bég**, & Khan, Z. H. (2016). MHD dissipative flow and heat transfer of Casson fluids due to metachronal wave propulsion of beating cilia with thermal and velocity slip effects under an oblique magnetic field. *Acta Astronautica*, *128*, 1-12.

27]. Hafeez, A., Khan, M., Ahmed, A., & Ahmed, J. (2020). Rotational flow of Oldroyd-B nanofluid subject to Cattaneo-Christov double diffusion theory. *Applied Mathematics and Mechanics*, *41*(7), 1083-1094.

28]. Rana, S., Mehmood, R., & Bhatti, M. M. (2021). Bioconvection oblique motion of magnetized Oldroyd-B fluid through an elastic surface with suction/injection. *Chinese Journal of Physics*, *73*, 314-330. https://doi.org/10.1016/j.cjph.2021.07.013

29]. Khan, S. U., Al-Khaled, K., & Bhatti, M. M. (2021). Bioconvection analysis for flow of Oldroyd-B nanofluid configured by a convectively heated surface with partial slip effects. *Surfaces and Interfaces*, *23*, 100982.[https://doi.org/ 10.1016/j.surfin. 2021.100982](https://doi.org/10.1016/j.surfin.2021.100982)

30]. Ali, B., Hussain, S., Nie, Y., Hussein, A. K., & Habib, D. (2021). Finite element investigation of Dufour and Soret impacts on MHD rotating flow of Oldroyd-B nanofluid over a stretching sheet with double diffusion Cattaneo Christov heat flux model. *Powder Technology*, *377*, 439-452.

31]. Irfan, M., Aftab, R., & Khan, M. (2021). Thermal performance of Joule heating in Oldroyd-B nanomaterials considering thermal-solutal convective conditions. *Chinese Journal of Physics*, *71*, 444-457. https://doi.org/10.1016/j.cjph.2021.03.010

32]. Yasir, M., Ahmed, A., Khan, M., Alzahrani, A. K., Malik, Z. U., & Alshehri, A. M. (2022). Mathematical modelling of unsteady Oldroyd-B fluid flow due to stretchable cylindrical surface with energy transport. *Ain Shams Engineering Journal*, 101825.

33]. S. Z. Abbas, W. A. Khan, M. Waqas, M. Irfan and Z. Asghar, Exploring the features for flow of Oldroyd-B liquid film subjected to rotating disk with homogeneous/heterogeneous processes, *Computer Methods and Programs in Biomedicine* 189 (2020) 105323.

34]. M. Waqas, T. Hayat, A. Alsaedi and W. A. Khan, Analytical evaluation of Oldroyd-B nanoliquid under thermo-solutal Robin conditions and stratifications, *Computer Methods and Programs in Biomedicine* 196 (2020) 105474.

35]. S. D. Gkormpatsis, K. D. Housiadas and A. N. Beris, Steady sphere translation in weakly viscoelastic UCM/Oldroyd-B fluids with perfect slip on the sphere, *European Journal of Mechanics-B/Fluids* 95 (2022) 335-346.

36]. J. Cui, S. Munir, S. F. Raies, U. Farooq and R. Razzaq, Non-similar aspects of heat generation in bioconvection from flat surface subjected to chemically reactive stagnation point flow of Oldroyd-B fluid, *Alexandria Engineering Journal* 61 (2022) 5397-5411.

37]. S. Saha and B. Kundu, Electroosmotic pressure-driven oscillatory flow and mass transport of Oldroyd-B fluid under high zeta potential and slippage conditions in microchannels, *Colloids and Surfaces A: Physicochemical and Engineering Aspects* 647 (2022) 129070.

38]. M. Nasir, M. Waqas, **O. Anwar Bég**, D. B. Basha, N. Zamri, H. J. Leonard and I. Khan, Chemically reactive Maxwell nanoliquid flow by a stretching surface in the frames of Newtonian heating, nonlinear convection and radiative flux: Nanopolymer flow processing simulation, *Nanotechnology Reviews* 11 (2022) 1291-1306.

39]. Z. Asghar, N. Ali, K. Javid, M. Waqas, A. S. Dogonchi and W. A. Khan, Bio-inspired propulsion of micro-swimmers within a passive cervix filled with couple stress mucus, *Computer Methods and Programs in Biomedicine* 189 (2020) 105313.

40]. Z. Asghar, R. A. Shah, A. A. Pasha, M. M. Rahman and M. W. S. Khan, Controlling kinetics of self-propelled rod-like swimmers near multi sinusoidal substrate, Controlling kinetics of self-propelled rod-like swimmers near multi sinusoidal substrate, *Computers in Biology and Medicine* 151 (2022) 106250.

41]. K. Guedri, M. M. A. Lashin, A. Abbasi, S. U. Khan, E. S. M. Tag-ElDin, M. I. Khan, F. Khalil and A. M. Galal, Modeling and mathematical investigation of blood-based flow of compressible rate type fluid with compressibility effects in a microchannel, *Micromachines* (2022) DOI: 10.3390/mi13101750.

42]. Z. Asghar, R. A. Shah, W. Shatanawi and N. Ali, FENE-P fluid flow generated by self-propelling bacteria with slip effects, *Computers in Biology and Medicine* (2022) DOI: 10.1016/j.compbiomed.2022.106386

43]. A. S. Dogonchi, M. Waqas, S. R. Afshar, S. M. Seyyedi, M. H. Tilehnoee, A. J. Chamkha and D. D. Ganji, Investigation of magneto-hydrodynamic fluid squeezed between two parallel disks by considering Joule heating, thermal radiation, and adding different nanoparticles, *International Journal of Numerical Methods for Heat & Fluid Flow* 30 (2020) 659-680.

44]. A. S. Dogonchi, S. R. Mishra, A. J. Chamkha, M. Ghodrat, Y. Elmasry and H. Alhumade, Thermal and entropy analyses on buoyancy-driven flow of nanofluid inside a porous enclosure with two square cylinders: Finite element method, *Case Studies in Thermal Engineering* 27 (2021) 101298.

45]. Z. Asghar, M. Waqas, M. A. Gondal and W. A. Khan, Electro-osmotically driven generalized Newtonian blood flow in a divergent micro-channel, *Alexandria Engineering Journal* 61 (2022) 4519-4528.

46]. R. A. Shah, Z. Asghar and N. Ali, Mathematical modeling related to bacterial gliding mechanism at low Reynolds number with Ellis slime, *The European Physical Journal Plus* 137 (2022) 1-12.

47]. K. Javid, Z. Asghar, U. Saeed and M. Waqas, Porosity effects on the peristaltic flow of biological fluid in a complex wavy channel, *Pramana* 96 (2022) 1-13.

48]. Liao, S. (2003). *Beyond Perturbation: Introduction to the Homotopy Analysis Method*. Chapman and Hall/CRC, https://doi.org/10.1201/9780203164

49]. Abbasi, F. M., Mustafa, M., Shehzad, S. A., Alhuthali, M. S., & Hayat, T. (2015). Analytical study of Cattaneo–Christov heat flux model for a boundary layer flow of Oldroyd-B fluid. *Chinese Physics B, 25*(1), 014701, https://doi.org/10.1088/1674-1056/25/1/014701.

50]. Khan, M., Yasir, M., Alshomrani, A. S., Sivasankaran, S., Aladwani, Y. R., & Ahmed, A. (2022). Variable heat source in stagnation-point unsteady flow of magnetized Oldroyd-B fluid with cubic autocatalysis chemical reaction. *Ain Shams Engineering Journal*, *13*(3), 101610.

51]. Haupt, K.; Mosbach, K. (2000). Molecularly imprinted polymers and their use in biomimetic sensors. *Chem. Rev. 100*, 2495–2504.

52]. Stolov, A.A.; Wrubel, J.A.; Simoff, D.A. (2016). Thermal stability of specialty optical fiber coatings. *J. Therm. Anal. Calorim*. 2016, 124, 1411–1423.

53]. Rivero, P.J.; Goicoechea, J.; Arregui, F.J. (2018). Optical fiber sensors based on polymeric sensitive coatings. *Polymers*, 10, 280.

54]. K. M. Sivaraman *et al*., (2013). Functional polypyrrole coatings for wirelessly controlled magnetic microrobots, *2013 IEEE Point-of-Care Healthcare Technologies (PHT)*, 2013, 22-25.

55]. J. Yang *et al.*, (2022). Conformal surface-nanocoating strategy to boost high-performance film cathodes for flexible zinc-ion batteries as an amphibious soft robot, *Energy Storage Materials***, 46,** 472-481.